www.sciencemag.org/cgi/content/full/science.aar5836/DC1

Supplementary Materials for

Abrupt cloud clearing of marine stratocumulus in the subtropical southeast Atlantic

Sandra E. Yuter*, John D. Hader, Matthew A. Miller, David. B. Mechem

*Corresponding author. Email: seyuter@ncsu.edu

Published 19 July 2018 on *Science* First Release
DOI: 10.1126/science.aar5836

This PDF file includes:

Other Supplementary Material for this manuscript includes the following:
(available at www.sciencemag.org/cgi/content/full/science.aar5836/DC1)

Movies S1 to S6

Materials and Methods

We use both polar-orbiting and geosynchronous satellite data in our analysis. A primary data set is the Moderate Resolution Imaging Spectroradiometer (MODIS) corrected reflectance true color data from the NASA Aqua and Terra satellites (*42*). We also examined MODIS Merged Dark Target/Deep Blue Aerosol Optical Depth (*43*) and Suomi-National Polar orbiting Partnership (Suomi-NPP) satellite Visible Infrared Imaging Radiometer Suite (VIIRS) corrected reflectance imagery. These data were obtained from NASA's Earth Observing System Data and Information System (EOSDIS) Worldview tool (*38*). The MODIS instrument has a swath width of 2330 km. The corrected reflectance data have an approximate pixel size of 250 m. The sun-synchronous orbits of the Terra and Aqua satellites result in data over the subtropical southeast Atlantic twice daily during daylight hours at roughly 10:30 LT (Terra) and 13:30 LT (Aqua) (MODIS). The Suomi-NPP satellite VIIRS corrected reflectance product is daylight only at roughly 13:30 LT and is provided at 250 meters resolution. The swath width is 3000 km. Along the southwestern African coast, the local time is one hour ahead of UTC, while the area further west near St. Helena Island (-15.9° latitude, -5.7° longitude), the local time aligns with UTC. For simplicity, we ignore the small discrepancy between UTC time and local time in the region of interest.

Short time-scale and short spatial-scale features of the marine stratocumulus erosion during daylight hours were examined using High Rate Spinning Enhanced Visible and IR Imager (SEVIRI) Level 1.5 visible satellite data from the Meteosat-10 geosynchronous satellite (centered at 0°latitude, 0°longitude). These data were obtained from the European Organization for the Exploitation of Meteorological Satellites (EUMETSAT) (*39*). Meteosat full-Earth scans are available roughly every 15 minutes with a pixel size between 3.1 and 4 km in the region of interest. Three-channel visible and near-infrared images using the 0.6 μm, 0.8 μm, and 1.6 μm channels were retrieved from the EUMETSAT Earth Observing Portal (*39*).

Half-hourly global merged infrared satellite data were obtained from NASA's Goddard Earth Sciences Data and Information Services Center (GES DISC) (*40)*. This merged infrared product is created by combining brightness temperature data from multiple geostationary satellites into a globally-complete brightness temperature data set on a uniform global grid with a pixel size of ≈4 km (*44*). The geosynchronous IR data are used to examine the brightness temperatures over the southeast Atlantic and southern Africa throughout the diurnal cycle.

Data from the Modern-Era Retrospective Analysis for Research and Application (MERRA) (*45*) were obtained through NASA's GES DISC. We used the 3-hourly instantaneous fields with a grid spacing of 0.5° latitude by 0.625° longitude, for the period 01 January 2000 through 31 December 2015. Monthly averages of 700 hPa pressure vertical velocity were computed from the daily-averaged meteorological variables to facilitate comparisons among different calendar months.

A sharp cloudiness transition boundary is defined as an abrupt transition (typically ≤10 km) between visually obvious regions of nearly overcast conditions to either decreased cloudiness or complete clearing (*37*). Our definition of a westward-moving cloudiness transition specifies that the boundary has to be at least 200 km in

length (≈2° latitude/longitude) and have a predominantly westward component of motion. In accordance with the latter criterion, most of the boundaries were oriented roughly in a north-south direction. We used visual examination of pairs of satellite images to tabulate days on which at least one westward-moving cloudiness transition occurred during the period from 8 May 2012 through 31 July 2017 in the region bounded by 10°S and 20°S latitude and 0° and 12°E longitude. Eight different analysts participated in examining the set of pairs of MODIS Aqua and Terra corrected reflectance images for each day (subsequently referred to as a 'cloud scene pair'). Each person was trained on the specific visual cues required to identify and categorize the boundaries and performed supervised practice on real examples before conducting the actual analysis. Most individuals analyzed 10-12 months of cloud scene pairs. To mitigate potential classification biases among individual analysts, cloud scene pairs for each day were analyzed by at least two people. The Terra and Aqua overpasses were analyzed in tandem to ascertain the movement of the boundary between the two overpasses (≈3 hours apart). When available, Suomi-NPP data were used to observe areas that fell in the gaps between Aqua MODIS swaths. The daily cloud scene pairs were categorized as definitely having a sharp cloudiness transition present ('yes'), definitely not having a sharp cloudiness transition present ('no'), or possibly having a sharp cloudiness transition present ('maybe'). In instances where the swath of the MODIS instrument missed a portion of the cloud deck, a 'yes', 'no', or 'maybe' decision was still made with the available information.

After this first round of cloud scene pair categorization, the two or more decisions for each cloud scene pair were compared. Scenes for which all analysts agreed on either a 'yes' or 'no' categorization were placed into the respective categories. For instances in which the analyzers disagreed or at least one analyzer indicated a 'maybe' categorization, the cloud scene pair was subsequently analyzed by two experienced satellite imagery analysts to determine if their categorization as 'yes', 'no', or 'maybe' could be resolved. For the 1911-day data set, there was a total of 377 'yes' days (days with a boundary present), 109 'maybe' days, and 1425 'no' days.

We consider the 'yes' subset of cloud scene pairs a robust underestimate of the actual number of cloudiness transitions that occur since it does not take into account multiple boundaries occurring on a single day or the 'maybe' category. Subjective analysis of satellite images to determine the occurrence frequency of atmospheric gravity waves has previously been done many times in the literature (*26, 28, 31, 46*).

A combination of Hovmöller diagrams based on Meteosat IR plus Aqua and Terra corrected reflectance image pairs were used to estimate the westward speed of the cloudiness transitions. We estimated speeds using several dozen pairs of Aqua and Terra images and about a dozen Hovmöller diagrams. Hovmöller diagrams of the satellite data were generated for the region between 6°W to 11°E longitude and 12.5°S to 17.5°S latitude (Fig. 3B). Brightness temperature values and corrected reflectance values within the analysis region were averaged meridionally for each 30-min and 15-min time step respectively.

Supplementary text

Propagating lines of clouds associated with atmospheric gravity waves occur in many locations throughout the world including the Morning Glory over the Gulf of Carpenteria (*28, 29, 47-49*), the northwest coast of Australia (*26*), the Mozambique Channel between Africa and Madagasar (*31*), the western Gulf of Mexico (*32*), and the Arabian Sea (*30, 50*). Similar dynamics have been documented in gravity waves that do not produce lines of clouds over the Red Sea (*46*), in Alabama (*51*), and over the Los Angeles Basin (*52*). The wave-cloud lines are all associated with increases in boundary layer height from either single solitary waves, solitary wave packets, and/or bores. The interaction between a density current and a stable layer can generate a leading undular bore and a trailing set of solitary waves that together raise the height of the boundary layer for several hours (*32, 35*).

Data from microbaragraph and infrasonic arrays in northwest Australia illustrated that waves of elevation were much more common than those of depression in that region (*53*). Over a two-year period, 99 solitary waves of elevation were observed compared to only 3 'down-up' single solitary waves of depression (*53*). The waves of depression occurred in clear skies and from their phase speed characteristics were inferred to be high altitude rather than boundary layer structures.

The observed westward speed of motion of the cloud-eroding boundaries, as derived from the Hovmöller diagrams of IR and visible geosynchronous satellite data as well as the Terra and Aqua MODIS corrected reflectance overpasses, was found to be 8-12 ms^{-1}. To compare this observed speed to theory, we calculated the intrinsic gravity wave phase speed of the environment (*54*):

$$c = \frac{N}{\sqrt{(\frac{2\pi}{L_x})^2 + (\frac{2\pi}{L_z})^2}} \quad (1)$$

where N is the Brunt Väisälä frequency, and L_x and L_z are the horizontal and vertical wavelengths. Horizontal wavelengths of 2, 5, and 8 km are estimated based on observations of wave features along the cloud-eroding boundaries in Terra and Aqua MODIS corrected reflectance images. Given the dearth of operational upper sounding stations along the southwest African coasts of Nambia and Angola, we used upper air soundings from St. Helena Island, the nearest operational sounding station which is 1800 km from coast of Africa, (*55*) to estimate inversion height and Brunt Väisälä frequency characteristics. We used the subset of soundings from 2000 through 2011 that exhibited a strong inversion (i.e. a change in potential temperature of at least 8 K within a 300 m layer) and were obtained in an environment where the daily average lower tropospheric stability between -5.625° and -16° longitude (from MERRA reanalysis data) varied by 3 K or less (i.e., they were obtained in conditions where the environment at St. Helena Island was expected to be reasonably representative of the region adjacent to the African coast). This analysis yielded estimated maximum and minimum values of the Brunt Väisälä frequency of 0.052 s^{-1} and 0.04 s^{-1}. We used 1.75 km, the median inversion height from St. Helena Island in January as an estimated upper bound, and 1 km, the cloud top heights observed adjacent to the African coast during austral spring (*56*) as an estimated lower bound for the vertical wavelengths. The resulting intrinsic gravity wave phase speeds for the combinations of these parameters range from 5.7 to 14.1 ms^{-1} (Table S1)

Table S1: Intrinsic gravity wave phase speeds for various parameter values (in ms^{-1}). L_x denotes horizontal wavelength, L_z denotes vertical wavelength, and N denotes Brunt Väisälä frequency.

L_X (km)	$N = 0.04\ s^{-1}$ $L_Z = 1$ km	$N = 0.04\ s^{-1}$ $L_Z = 1.75$ km	$N = 0.052\ s^{-1}$ $L_Z = 1$ km	$N = 0.052\ s^{-1}$ $L_Z = 1.75$ km
2	5.7	8.4	7.4	10.9
5	6.2	10.5	8.1	13.7
8	6.3	10.9	8.2	14.1

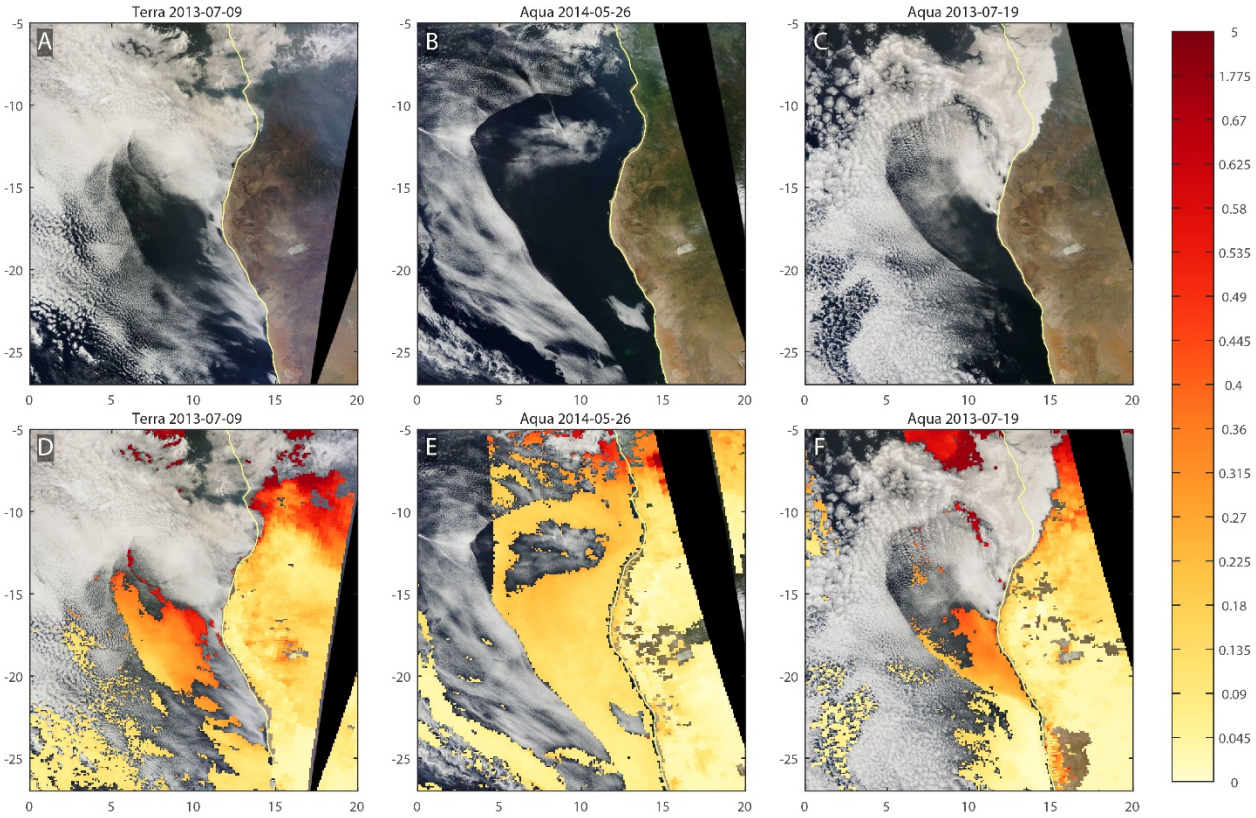

Fig. S1: Examples of cloud clearing events with corresponding aerosol optical depth estimates. MODIS Corrected Reflectance images for abrupt cloudiness transition events over the southeast Atlantic from (A) Terra on 9 July 2013, (B) Aqua on 26 May 2014, and (C) Aqua on 19 July 2013. (D, E, and F) The corresponding MODIS Merged Dark Target/Deep Blue Aerosol Optical Depth data overlaid on the MODIS Corrected Reflectance images.

Movie S1: Movie of 15-minute Meteosat visible imagery for 26 May 2014 from 05:00 to 18:15 UTC showing (left) regional view off the southwest coast of Africa and (right) close-up view corresponding to the yellow box on the left.

Movie S2: Movie of 30-minute merged infrared 12 μm brightness temperatures for the period from 25 May 2014 00:00 UTC to 27 May 2014 23:30 UTC showing a regional view of southern Africa and the southeast Atlantic. Red denotes missing data.

Movie S3: Movie of 15-minute Meteosat visible imagery for 26 May 2012 from 05:00 to 17:15 UTC showing (left) regional view off the southwest coast of Africa and (right) close-up view corresponding to the yellow box on the left.

Movie S4: Movie of 30-minute merged infrared 12 μm brightness temperatures for the period from 25 May 2012 00:00 UTC to 27 May 2012 23:30 UTC showing a regional view of southern Africa and the southeast Atlantic. Red denotes missing data.

Movie S5: Movie of 15-minute Meteosat visible imagery for 12 May 2015 from 05:00 to 17:45 UTC showing (left) regional view off the southwest coast of Africa and (right) close-up view corresponding to the yellow box on the left.

Movie S6: Movie of 30-minute merged infrared 12 μm brightness temperatures for the period from 11 May 2015 00:00 UTC to 13 May 2015 23:30 UTC showing regional view of southern Africa and the southeast Atlantic. Red denotes missing data.

References and Notes

1. D. L. Hartmann, M. E. Ockert-Bell, M. L. Michelsen, The effect of cloud type on Earth's energy balance: Global analysis. *J. Clim.* **5**, 1281–1304 (1992). doi:10.1175/1520-0442(1992)005<1281:TEOCTO>2.0.CO;2

2. C. S. Bretherton, T. Uttal, C. W. Fairall, S. E. Yuter, R. A. Weller, D. Baumgardner, K. Comstock, R. Wood, G. B. Raga, The EPIC 2001 Stratocumulus Study. *Bull. Am. Meteorol. Soc.* **85**, 967–978 (2004). doi:10.1175/BAMS-85-7-967

3. W. H. Schubert, J. S. Wakefield, E. J. Steiner, S. K. Cox, Marine stratocumulus convection. Part I: Governing equations and horizontally homogeneous solutions. *J. Atmos. Sci.* **36**, 1286–1307 (1979). doi:10.1175/1520-0469(1979)036<1286:MSCPIG>2.0.CO;2

4. B. Stevens, Entrainment in stratocumulus-topped mixed layers. *Q. J. R. Meteorol. Soc.* **128**, 2663–2690 (2002). doi:10.1256/qj.01.202

5. B. Stevens, W. R. Cotton, G. Feingold, C.-H. Moeng, Large-eddy simulations of strongly precipitating, shallow, stratocumulus-topped boundary layers. *J. Atmos. Sci.* **55**, 3616–3638 (1998). doi:10.1175/1520-0469(1998)055<3616:LESOSP>2.0.CO;2

6. A. S. Ackerman, M. C. vanZanten, B. Stevens, V. Savic-Jovcic, C. S. Bretherton, A. Chlond, J.-C. Golaz, H. Jiang, M. Khairoutdinov, S. K. Krueger, D. C. Lewellen, A. Lock, C.-H. Moeng, K. Nakamura, M. D. Petters, J. R. Snider, S. Weinbrecht, M. Zulauf, Large-eddy simulations of a drizzling, stratocumulus-topped marine boundary layer. *Mon. Weather Rev.* **137**, 1083–1110 (2009). doi:10.1175/2008MWR2582.1

7. R. Wood, C. S. Bretherton, D. Leon, A. D. Clarke, P. Zuidema, G. Allen, H. Coe, An aircraft case study of the spatial transition from closed to open mesoscale cellular convection over the Southeast Pacific. *Atmos. Chem. Phys.* **11**, 2341–2370 (2011). doi:10.5194/acp-11-2341-2011

8. I. Sandu, B. Stevens, On the factors modulating the stratocumulus to cumulus transitions. *J. Atmos. Sci.* **68**, 1865–1881 (2011). doi:10.1175/2011JAS3614.1

9. A. H. Berner, C. S. Bretherton, R. Wood, A. Muhlbauer, Marine boundary layer cloud regimes and POC formation in a CRM coupled to a bulk aerosol scheme. *Atmos. Chem. Phys.* **13**, 12549–12572 (2013). doi:10.5194/acp-13-12549-2013

10. S. P. de Szoeke, K. L. Verlinden, S. E. Yuter, D. B. Mechem, The time scales of variability of marine low clouds. *J. Clim.* **29**, 6463–6481 (2016). doi:10.1175/JCLI-D-15-0460.1

11. C. Brunet, R. Casotti, V. Vantrepotte, Phytoplankton diel and vertical variability in photobiological responses at a coastal station in the Mediterranean Sea. *J. Plankton Res.* **30**, 645–654 (2008). doi:10.1093/plankt/fbn028

12. C. M. Risien, D. B. Chelton, A global climatology of surface wind and wind stress fields from eight years of QuikSCAT Scatterometer data. *J. Phys. Oceanogr.* **38**, 2379–2413 (2008). doi:10.1175/2008JPO3881.1

13. S. A. Klein, Synoptic variability of low-cloud properties and meteorological parameters in the subtropical trade wind boundary layer. *J. Clim.* **10**, 2018–2039 (1997). doi:10.1175/1520-0442(1997)010<2018:SVOLCP>2.0.CO;2

14. M. A. Rozendaal, W. B. Rossow, Characterizing some of the influences of the general circulation on subtropical marine boundary layer clouds. *J. Atmos. Sci.* **60**, 711–728 (2003). doi:10.1175/1520-0469(2003)060<0711:CSOTIO>2.0.CO;2

15. R. C. George, R. Wood, Subseasonal variability of low cloud radiative properties over the southeast Pacific Ocean. *Atmos. Chem. Phys.* **10**, 4047–4063 (2010). doi:10.5194/acp-10-4047-2010

16. N.-C. Lau, M. W. Crane, A satellite view of the synoptic-scale organization of cloud properties in midlatitude and tropical circulation systems. *Mon. Weather Rev.* **123**, 1984–2006 (1995). doi:10.1175/1520-0493(1995)123<1984:ASVOTS>2.0.CO;2

17. S. A. Klein, C. Jakob, Validation and sensitivities of frontal clouds simulated by the ECMWF model. *Mon. Weather Rev.* **127**, 2514–2531 (1999). doi:10.1175/1520-0493(1999)127<2514:VASOFC>2.0.CO;2

18. G. L. Stephens, Cloud feedbacks in the climate system: A critical review. *J. Clim.* **18**, 237–273 (2005). doi:10.1175/JCLI-3243.1

19. E. Crosbie, Z. Wang, A. Sorooshian, P. Y. Chuang, J. S. Craven, M. M. Coggon, M. Brunke, X. Zeng, H. Jonsson, R. K. Woods, R. C. Flagan, J. H. Seinfeld, Stratocumulus cloud clearings and notable thermodynamic and aerosol contrasts across the clear cloudy interface. *J. Atmos. Sci.* **73**, 1083–1099 (2016). doi:10.1175/JAS-D-15-0137.1

20. R. Garreaud, R. Muñoz, The diurnal cycle in circulation and cloudiness over the subtropical southeast Pacific: A modeling study. *J. Clim.* **17**, 1699–1710 (2004). doi:10.1175/1520-0442(2004)017<1699:TDCICA>2.0.CO;2

21. C. W. O'Dell, F. J. Wentz, R. Bennartz, Cloud liquid water path from satellite-based passive microwave observations: A new climatology over the global oceans. *J. Clim.* **21**, 1721–1739 (2008). doi:10.1175/2007JCLI1958.1

22. R. Wood, M. Köhler, R. Bennartz, C. O'Dell, The diurnal cycle of surface divergence over the global oceans. *Q. J. R. Meteorol. Soc.* **135**, 1484–1493 (2009). doi:10.1002/qj.451

23. G. Allen, G. Vaughan, T. Toniazzo, H. Coe, P. Connolly, S. E. Yuter, C. D. Burleyson, P. Minnis, J. K. Ayers, Gravity-wave-induced perturbations in marine stratocumulus. *Q. J. R. Meteorol. Soc.* **139**, 32–45 (2013). doi:10.1002/qj.1952

24. P. J. Connolly, G. Vaughan, P. Cook, G. Allen, H. Coe, T. W. Choularton, C. Dearden, A. Hill, Modelling the effects of gravity waves on stratocumulus clouds observed during VOCALS-UK. *Atmos. Chem. Phys.* **13**, 7133–7152 (2013). doi:10.5194/acp-13-7133-2013

25. S. A. Klein, D. L. Hartmann, The seasonal cycle of low stratiform clouds. *J. Clim.* **6**, 1587–1606 (1993). doi:10.1175/1520-0442(1993)006<1587:TSCOLS>2.0.CO;2

26. C. E. Birch, M. J. Reeder, Wave-cloud lines over northwest Australia. *Q. J. R. Meteorol. Soc.* **139**, 1311–1326 (2013). doi:10.1002/qj.2043

27. B. E. Mapes, Gregarious tropical convection. *J. Atmos. Sci.* **50**, 2026–2037 (1993). doi:10.1175/1520-0469(1993)050<2026:GTC>2.0.CO;2

28. R. H. Clarke, R. K. Smith, D. G. Reid, The morning glory of the Gulf of Carpentaria: An atmospheric undular bore. *Mon. Weather Rev.* **109**, 1726–1750 (1981). doi:10.1175/1520-0493(1981)109<1726:TMGOTG>2.0.CO;2

29. D. R. Christie, K. J. Muirhead, R. H. Clarke, Solitary waves in the lower atmosphere. *Nature* **293**, 46–49 (1981). doi:10.1038/293046a0

30. F. Désalmand, A. Szantai, L. Picon, M. Desbois, Systematic observation of westward propagating cloud bands over the Arabian Sea during Indian Ocean Experiment (INDOEX) from Meteosat-5 data. *J. Geophys. Res.* **108** (D18), 8004 (2003). doi:10.1029/2002JD002934

31. J. C. B. da Silva, J. M. Magalhaes, Satellite observations of large atmospheric gravity waves in the Mozambique Channel. *Int. J. Remote Sens.* **30**, 1161–1182 (2009). doi:10.1080/01431160802448943

32. P. A. Lutzak, A proposal for analyzing and forecasting lower-atmospheric undular bores in the western Gulf of Mexico region. *Weather Forecast.* **28**, 55–76 (2013). doi:10.1175/WAF-D-12-00051.1

33. T. Qian, C. C. Epifanio, F. Zhang, Topographic effects on the tropical land and sea breeze. *J. Atmos. Sci.* **69**, 130–149 (2012). doi:10.1175/JAS-D-11-011.1

34. S. T. Gille, Global observations of the land breeze. *Geophys. Res. Lett.* **32**, L05605 (2005). doi:10.1029/2004GL022139

35. S. E. Koch, W. Feltz, F. Fabry, M. Pagowski, B. Geerts, K. M. Bedka, D. O. Miller, J. W. Wilson, Turbulent mixing processes in atmospheric bores and solitary waves deduced from profiling systems and numerical simulation. *Mon. Weather Rev.* **136**, 1373–1400 (2008). doi:10.1175/2007MWR2252.1

36. C. D. Burleyson, S. E. Yuter, Subdiurnal stratocumulus cloud fraction variability and sensitivity to precipitation. *J. Clim.* **28**, 2968–2985 (2015). doi:10.1175/JCLI-D-14-00648.1

37. J. Hader, "Propagating, cloud-eroding boundaries in southeast Atlantic marine stratocumulus," thesis, North Carolina State University, Raleigh, NC (2016).

38. NASA, EOSDIS Worldview; https://worldview.earthdata.nasa.gov/.

39. EUMETSAT Product Navigator, http://navigator.eumetsat.int/.

40. J. Janowiak, B. Joyce, P. Xie, NCEP/CPC L3 half hourly 4km global (60S - 60N) merged IR V1, A. Savtchenko, Ed. [Goddard Earth Sciences Data and Information Services Center (GES DISC), 2017]; http://dx.doi.org/10.5067/P4HZB9N27EKU.

41. S. E. Yuter, Southeast Atlantic westward-moving cloud erosion boundaries, Open Science Framework (2018); doi:10.17605/OSF.IO/KR4JS.

42. NASA, MODIS; http://modis.gsfc.nasa.gov/about/specifications.php.

43. R. C. Levy, S. Mattoo, L. A. Munchak, L. A. Remer, A. M. Sayer, F. Patadia, N. C. Hsu, The Collection 6 MODIS aerosol products over land and ocean. *Atmos. Meas. Tech.* **6**, 2989–3034 (2013). doi:10.5194/amt-6-2989-2013

44. J. E. Janowiak, R. J. Joyce, Y. Yarosh, A real time global half hourly pixel resolution infrared dataset and its applications. *Bull. Am. Meteorol. Soc.* **82**, 205–217 (2001). doi:10.1175/1520-0477(2001)082<0205:ARTGHH>2.3.CO;2

45. M. M. Rienecker, M. J. Suarez, R. Gelaro, R. Todling, J. Bacmeister, E. Liu, M. G. Bosilovich, S. D. Schubert, L. Takacs, G.-K. Kim, S. Bloom, J. Chen, D. Collins, A. Conaty, A. da Silva, W. Gu, J. Joiner, R. D. Koster, R. Lucchesi, A. Molod, T. Owens, S. Pawson, P. Pegion, C. R. Redder, R. Reichle, F. R. Robertson, A. G. Ruddick, M. Sienkiewicz, J. Woollen, MERRA: NASA's modern-era retrospective analysis for research and applications. *J. Clim.* **24**, 3624–3648 (2011). doi:10.1175/JCLI-D-11-00015.1

46. J. M. Magalhaes, I. B. Araújo, J. C. B. da Silva, R. H. J. Grimshaw, K. Davis, J. Pineda, Atmospheric gravity waves in the Red Sea: A new hotspot. *Nonlinear Process. Geophys.* **18**, 71–79 (2011). doi:10.5194/npg-18-71-2011

47. R. H. Clarke, The morning glory: An atmospheric hydraulic jump. *J. Appl. Meteorol.* **11**, 304–311 (1972). doi:10.1175/1520-0450(1972)011<0304:TMGAAH>2.0.CO;2

48. D. R. Christie, The morning glory of the Gulf of Carpentaria: A paradigm for nonlinear waves in the lower atmosphere. *Aust. Meteorol. Mag.* **41**, 21–60 (1992).

49. R. K. Smith, G. Roff, N. Crook, The morning glory: An extraordinary atmospheric undular bore. *Q. J. R. Meteorol. Soc.* **108**, 937–956 (1982). doi:10.1002/qj.49710845813

50. C. E. Birch, M. J. Reeder, G. J. Berry, Wave-cloud lines over the Arabian Sea. *J. Geophys. Res. Atmos.* **119**, 4447–4457 (2014). doi:10.1002/2013JD021347

51. T. A. Coleman, K. R. Knupp, Radiometer and profiler analysis of the effects of a bore and a solitary wave on the stability of the nocturnal boundary layer. *Mon. Weather Rev.* **139**, 211–223 (2011). doi:10.1175/2010MWR3376.1

52. V. C. Tsai, H. Kanamori, J. Artru, The morning glory wave of southern California. *J. Geophys. Res. Solid Earth* **109** (B2), (2004). doi:10.1029/2003JB002596

53. D. R. Christie, K. J. Muirhead, A. L. Hales, On solitary waves in the atmosphere. *J. Atmos. Sci.* **35**, 805–825 (1978). doi:10.1175/1520-0469(1978)035<0805:OSWITA>2.0.CO;2

54. J. R. Holton, G. J. Hakim, *An Introduction to Dynamic Meteorology* (Elsevier, 2013).

55. A. A. Adebiyi, P. Zuidema, S. J. Abel, The convolution of dynamics and moisture with the presence of shortwave absorbing aerosols over the southeast Atlantic. *J. Clim.* **28**, 1997–2024 (2015). doi:10.1175/JCLI-D-14-00352.1

56. D. Painemal, S. Kato, P. Minnis, Boundary layer regulation in the southeast Atlantic cloud microphysics during the biomass burning season as seen by the A-train satellite constellation. *J. Geophys. Res. Atmos.* **119**, 11,288–11,302 (2014). doi:10.1002/2014JD022182